

Energy redistribution dynamics in coupled Couette–Poiseuille flows using large-Eddy simulation

Santiago López Castaño^{*,a,1}, Bernard J. Geurts^{b,c}, Vincenzo Armenio^a

^a Department of Engineering & Architecture, University of Trieste, Via Valerio 1, Italy

^b Engineering Physics and Mathematics, Faculty EEMCS, University of Twente, P.O. Box 217, AE Enschede 7500, The Netherlands

^c Multiscale Physics of Energy Systems, CCER - Eindhoven University of Technology, P.O. Box 513, MB Eindhoven 5600, The Netherlands

ARTICLE INFO

Keywords:

Air/water interface
Wind/ocean dynamics
LES Of coupled flows
Coupled Poiseuille–Couette flows

ABSTRACT

The problem of turbulent Couette flow driven by a statistically steady external wind is studied in the framework of spatially filtered Navier–Stokes equations. The phenomenon of wind-driven flow of water is represented by a layer of air modeled as Poiseuille flow (air sub-domain), coupled to a layer of water modeled as Couette flow (water sub-domain). We focus on changes in the statistics in either the air or the water sub-domain, due to the coupling with the other sub-domain. We also highlight dynamic flow structures forming near the air–water interface. Simulations based on different *Reynolds numbers* in the air and the water sub-domains are compared to computationally less demanding simulations with equal Reynolds numbers. Results of these simulations indicate strong similarities, i.e., the flow is well approximated by simulating air and water at the same Reynolds numbers. Further analysis shows that the flow in the water domain shares important features with classical Couette flows. The horizontal turbulent mixing renders a thinner boundary layer in the water sub-domain. Moreover, an increased intermittency in the flow velocities is observed, which may be linked to so-called splat events near the air–water interface. These splats characterize the interaction of coherent structures across the interface, being stronger in the water phase. An analysis of the pressure–strain correlation near the air–water interface on the water side shows that such splats are responsible for redistributing energy from the streamwise and spanwise directions, to the vertical direction. This behavior, although qualitatively similar to wall-bounded flows, differ mainly on the fact that most of the energy drained comes from the streamwise direction: in wall-bounded the main contributor is the spanwise direction. The boundary layers near the air–water interface show inclined vortical structures. Unlike in coupled Couette–Couette flow, the peak in the Reynolds stress is displaced from the channel's center into the buffer region of the water sub-domain.

1. Introduction

Wind-driven flow at the interface between air and water is of central importance to many natural and technological problems. For example, near-surface mixing and stratification in pre-Alpine lakes are mainly driven by winds (Lorke and Wüest, 2003). Likewise, the turbulent Ekman layer in the ocean is driven by the shear stress imposed by the wind (Zikanov et al., 2003), while Langmuir circulations are formed by the interaction between elongated coherent structures in the upper wavy ocean layer and the atmospheric boundary layer (Craik and Leibovich, 1976). Particular interest has been with the mixing properties of the turbulent flow that arises at such highly sheared interfaces (Fulgosi et al., 2003). In this paper, we consider a flat air–water surface and treat the two fluid layers using the canonical setting

of a Couette boundary layer forming at the water-side of the interface, as a consequence of the traction imposed by a Poiseuille boundary layer on the air-side of the interface. This particular configuration of a Couette–Poiseuille coupling constitutes the main novelty of this study, with particular relevance to physical oceanography and limnology, as well as meteorology. It is representative of flows that interact through a sheared interface across highly stratified non-miscible fluids. Similar cases have been studied (Liu et al., 2009) for the confluence of two boundary layers of the same type, e.g., Couette–Couette and Poiseuille–Poiseuille. In fact, the case of Poiseuille–Poiseuille coupling is a well-known model in oceanography for the interaction between the atmospheric boundary layer and the deep ocean, disregarding rotational effects (Lombardi et al., 1996). The present study of Couette–Poiseuille coupling is proposed for investigating the interaction

* Corresponding author.

E-mail addresses: santiago.lopezcastano@mow.vlaanderen.be (S. López Castaño), b.j.geurts@utwente.nl (B.J. Geurts), vi.armenio@gmail.com (V. Armenio).

¹ Current address: Flanders Hydraulics Research, Berchemlei 115, 2140 Antwerpen-Borgerhout, Belgium.

between a shallow sea and the atmospheric boundary layer.

Simulations of coupled air-water systems have been conducted for the study of heat/scalar transport across its interface at low Reynolds numbers. A recent account of Direct Numerical Simulation (DNS) of wind-driven coupled air-water systems is in Kurose et al. (1996), where wind-generated waves are resolved directly using an *Arbitrary Lagrangian Eulerian* technique. Phase-averaged statistics of turbulent flow quantities show that the wavy boundary layer developed on the air side is similar to that of an open channel boundary layer. The waves resulting from wind traction at a frictional Reynolds number $Re_\tau = 171$ are well within the capillary regime. The wavy boundary layer developed on the water side is accompanied by clear Langmuir circulations, with a Langmuir number in terms of the Stokes drift velocity u_s and the shear velocity u_τ given by $La = \sqrt{u_s/u_\tau} \approx 1/300$. A more exhaustive description of the statistics for turbulent flow quantities under a coupled wavy system is presented by Fulgosi et al. (2003), for a counter-current Poiseuille-Poiseuille air-water domain. In this reference the focus is on the statistics on the air side, where first- and second-order statistics show that the air-side boundary layer is very similar to that of an open channel flow. Recently we (Lopez Castano et al., 2018) extended the work of Fulgosi et al. (2003) to higher order statistics and focused on intermittency near the interface. It was shown that the near-interface fluctuations on the water side are responsible for the occurrence of strong backflow regions across the interface which reduce drag, even in the absence of explicitly resolved surface waves.

In this paper the flow in the bottom water channel resembles that of a Couette flow. The literature on DNS of Couette flow is not as abundant as for wall-bounded channel flows. One salient work by Bech et al. (1995) studies the structure of near-wall turbulence using simulation and laboratory experiments. It was shown that the structure of turbulence near the moving wall differs considerably from that observed in channels bounded by stationary walls. In fact, for the Couette-type flow the maximum Reynolds stress is not observed inside the buffer region. Instead, for Couette-type flow, the maximum Reynolds stress is found at the mid-plane of the channel. This implies a stronger influence of the core region of the flow on the boundary layer, increasing, e.g., the contribution of sweeping events on the Reynolds stresses while diminishing ejection motions in the wall region. In this respect, the work of Nagaosa (1999) focuses on the nature of interface-borne vortices and their role on energy redistribution, on a free-surface channel. There, it is found that two types of vortices exist in the free-surface region: (1) quasi-streamwise, and (2) free-surface attached vortices. Such coherent structures have also been detected in studies regarding coupled Poiseuille-Poiseuille (and Couette-Couette) flows Lopez Castano et al. (2018); Liu et al. (2009), in the latter studies the inclination of the vortices relative to the free-surface is higher and these are not only interface attached but may even pass across the interface. It will be shown that such vortices are responsible for the generation of splats towards the free surface.

Direct Numerical Simulation on coupled Couette-Poiseuille flows are quite scarce and are mostly focused on the study of passive/active scalar transfer (Kurose et al., 1996). Particularly, the work of Liu et al. (2009) studies coupled air-water systems in which different Reynolds numbers are used on the two sub-domains, that is $Re_\tau^{air} = 272$ and $Re_\tau^{water} = 120$. It is shown that rather large and quite persistent streaky structures form on the water side. These structures on the water side dominate turbulent fluctuations near the interface on either side. The question whether these structures are longer and more persistent due to the different Re_τ values used in the sub-domains, or due to the thinner interface boundary layer on the water side remains open and will be explored further below.

One salient study is that of Handler et al. (2001), reporting both physical and numerical experiments on air-water interface turbulence. This study reveals the role of rising fluid impacting the free surface from below (so-called splats). In the work of Handler et al. (2001) the numerical experiments concentrated on flow in the channel subject to

an imposed average streamwise traction, representative of the effect of wind. The dynamics of spanwise instantaneous stresses and vertical vorticity at the interface, affects the occurrence, inclination, and energy of near-interface structures. This is a recurring theme throughout this paper, extending the work (Handler et al., 2001).

In this paper we investigate the boundary layers formed in a coupled air-water Couette-Poiseuille system. In most simulations, the shear Reynolds number is kept equal on both the air and the water sides, and the interface is treated as flat. By setting the same Re_τ values in the two sub-domains we arrive at a computationally less expensive model, as the computational grids and time scales can be taken equal as well. Such simulations will be referred to as *Equal Reynolds Couette-Poiseuille* (ERCP) simulations. An additional *Disparate Reynolds Couette-Poiseuille* (DRCP) simulation is included to quantify the approximations implied when working with equal Re_τ in the two sub-domains. Specifically, Re_τ is kept equal in the Couette (water) part of both DRCP and ERCP simulations and altered appropriately in the Poiseuille (air) part in the DRCP. In addition, a driving pressure gradient is prescribed only on the air domain to define the Couette-Poiseuille flow. The dynamics of the boundary layer that forms in the water sub-domain shows a characteristic relationship between vertical vorticity, Reynolds shear stress, and energy redistribution at the interface – this will be explored in detail.

The paper is organized as follows. Section 2 introduces the description of the problem and the numerical approach used to solve the equations. Section 3 presents the central statistics of the flow, the well-known quadrant analysis, and the turbulent kinetic energy budgets. In addition, we focus on the similarities between DRCP and ERCP flows. Section 4 concerns the near-interface vorticity dynamics. Finally, conclusions are provided in Section 5.

2. Mathematical and numerical approach

In this Section we first introduce the problem in more detail (Section 2.1) and subsequently sketch the numerical approach (Section 2.2).

2.1. Problem description

A coupled Couette-Poiseuille flow is studied with a lower domain filled with water (Couette type) and an upper domain filled with air (Poiseuille type). The Couette flow domain is bounded from below by a wall boundary condition and the Poiseuille flow domain is bounded from above by a free slip boundary. The two sub-domains are coupled at the interface Γ , which is kept flat. The configuration is depicted in Fig. 1. The flow is considered to be periodic in both horizontal directions (x, z). The Couette flow in the lower sub-domain is driven indirectly, by interaction with the Poiseuille flow in the upper sub-domain, which, in turn is driven by an external wind, represented by a pressure gradient Π .

The water channel has dimensions $4\pi\delta \times 2\delta \times 2\pi\delta$, where δ is the half-height of the water domain. On the air side the domain has dimensions $4\pi\delta \times \delta \times 2\pi\delta$. The grid is vertically refined near all boundaries and near the interface to have a higher local resolution to capture the relevant scales in the boundary layers. In the ERCP simulations, the shear based Reynolds number is set to $Re_\tau \equiv u_\tau \delta / \nu = 171$ on both sub-domains. Here, the shear velocity is defined as $u_\tau = \sqrt{\tau_i / \rho_i}$ where ρ_i denotes the density of each of the comprising fluids. That is, for the air and water subdomains, two different shear velocities exist (Lombardi et al., 1996). By setting Re_τ equal on both sub-domains as in ERCP, a simplifying modification of the dynamics is introduced making the computations less demanding. On the other hand, in DRCP simulations we also consider $Re_{\tau,water} = 171$ but use the exact properties of air and water at standard operating conditions, implying $Re_{\tau,air} \approx 2.2Re_{\tau,water}$, as it will be shown in Section 3.5. This corresponds to $Re_{\tau,air} \approx 390$, which introduces additional resolution and numerical

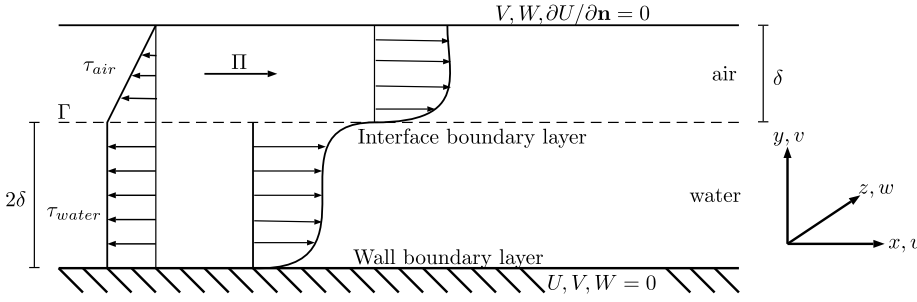


Fig. 1. Definition sketch of the coupled Couette-Poiseuille flow. The Poiseuille flow on top pertains to the air-filled region of height δ and is driven by a constant pressure gradient Π . The intersection between the sub-domains, Γ , is a flat interface, connecting to the water-filled lower domain of height 2δ in which a Couette-type setting is applied. The shear in the two layers is denoted by τ_{air} and τ_{water} respectively.

issues in DRCP over ERCP. However, the dynamical properties of the important water layer are expected to differ only by a small amount when replacing the more realistic DRCP air layer by the computationally less expensive ERCP air layer. In Section 3.5 we will establish this similarity between DRCP and ERCP in some detail, thereby underpinning the use of ERCP in the majority of simulations in this paper. The approximation of equal Reynolds numbers in different sub-domains was adopted by others before (Lombardi et al., 1996; Komori et al., 1993; Lopez Castano et al., 2018).

The governing equations for incompressible fluid flow are the filtered Navier-Stokes equations, written as

$$\frac{\partial \bar{u}_i}{\partial t} + \frac{\partial \bar{u}_j \bar{u}_i}{\partial x_j} = -\frac{1}{\rho_0} \frac{\partial \bar{P}}{\partial x_i} + \nu \frac{\partial^2 \bar{u}_i}{\partial x_k \partial x_k} - \frac{\partial \tau_{ij}}{\partial x_j} \quad (1)$$

$$\frac{\partial \bar{u}_i}{\partial x_i} = 0$$

where u_i , ρ_0 , P and τ_{ij} are the velocity, reference density of the fluid (air or water), pressure, and the *sub-grid scale* (SGS) fluxes resulting from the spatial filter (\cdot) . The filter is assumed to have size Δ and is applied on each of the fields, respectively, over the Cartesian coordinates ($x_1 = x$, $x_2 = y$, $x_3 = z$). By applying a second ‘test’ filter, $(\hat{\cdot})$ of size $\hat{\Delta} = 2\Delta$, first on Eq. (1) and then on the unfiltered version of the incompressible N-S Equations, the famous Germano identity (Germano, 1992) for the SGS fluxes on these filter scales is obtained:

$$\hat{\tau}_{ij} = T_{ij} - L_{ij} \quad (2)$$

$$L_{ij} = \bar{u}_i \bar{u}_j - \hat{u}_i \hat{u}_j \quad (3)$$

$$T_{ij} = \hat{u}_i \hat{u}_j - \bar{u}_i \bar{u}_j \quad (4)$$

where we identify a resolved term L_{ij} that can be evaluated from the LES solution, and the test-filtered SGS stress tensor T_{ij} . This identity is the basis for dynamic SGS modeling.

In this paper we use a mixed scale-similarity/Smagorinsky eddy-viscosity model m_{ij} to parameterize the unresolved anisotropic part of the SGS tensor:

$$\tau_{ij} \approx m_{ij} = (\bar{u}_i \bar{u}_j - \bar{u}_i \bar{u}_j) - 2c_s \Delta^2 |\bar{S}| \bar{S}_{ij} \quad (5)$$

where S denotes the rate of strain tensor and c_s is the ‘dynamic coefficient’ which can be extracted from a least squares optimization based on the Germano identity. The averaging needed in this approach is taken as time averages along Lagrangian paths, implying that we work with the Dynamic Lagrangian mixed SGS model in our simulations. For further details we refer to Armenio and Piomelli (2000).

The mathematical model implies that for each sub-domain the Navier-Stokes equations are solved separately using the appropriate fluid properties. For the coupling between the sub-domains, the normalized compatibility conditions for the incompressible Navier-Stokes equations at the interface are used. In vector form, these conditions are expressed as

$$((\tau_{water} - \tau_{air}) \cdot \mathbf{n}) \cdot \mathbf{n} + P_{air} - P_{water} = 0 \quad (6)$$

$$u_{air} = \frac{1}{\mathcal{R}} u_{water} \quad (7)$$

$$\mathcal{R} = \sqrt{\frac{\rho_{water}}{\rho_{air}}} \quad (8)$$

Where τ , P , ρ , and \mathbf{n} are the interface shear stress, dynamic (or thermodynamic) pressure, density, and interface-normal unit vector, respectively. Such compatibility conditions arise from *first principles* in continuum mechanics: a momentum balance at each side of the interface (neglecting surface tension) and the no penetration condition across two non-miscible media are enforced, leading to this coupling between shear stresses at the interface and pressure differences on both sides. Note that the momentum density ratio \mathcal{R} arises in the kinematic condition 7. If $\mathcal{R} = 1$ the velocities at the interface of air and water match.

2.2. Numerical approach

The incompressible, coupled, Navier-Stokes equations were numerically solved using COUPLEDLES which is an in-house second-order finite-difference code based on LES-COAST. LES-COAST solves the Navier-Stokes equations in curvilinear coordinates using a non-incremental pressure-correction algorithm (Zang et al., 1994). The code implements an immersed boundary technique (Roman et al., 2009), and has been used for the study of buoyant flows Armenio and Sarkar (2002) and coastal flows. Here, we use an incremental pressure projection method (Guermond and Shen, 2003; Lopez Castano et al., 2018) where the pressure gradient is considered in the momentum predictor step. For the coupling between the non-miscible fluids, the compatibility conditions 6 and 7 are enforced explicitly using fractional steps (Lopez Castano et al., 2018). The method is described in more detail in Lombardi et al. (1996).

3. Mean features of the flow

In this Section we use the ERCP setting and present various mean flow properties (Section 3.1), Reynolds stress budget (Section 3.2), higher order statistics (Section 3.3) and two-point correlations (Section 3.4) of the coupled Couette-Poiseuille flow. We also compare results obtained from ERCP with results derived from the more complete DRCP in Section 3.5 and show both their qualitative and quantitative similarity. This underpins the use of the computationally more effective ERCP for the analysis of the coupled flow, also in the sequel. Notice that in the case of DRCP, the computational grid on the water side would tend to be $O((\mathcal{R}))$ times finer than required for the corresponding Re_τ if one wants to avoid inter-grid interpolation across the fluid-gas interface. Also, the time step limit set by the CFL condition will be imposed in the air side which will be considerably less than the one required in the water side.

3.1. Mean velocities, reynolds stress, and TKE budget in ERCP flow

The statistical averages presented here are collected over a time

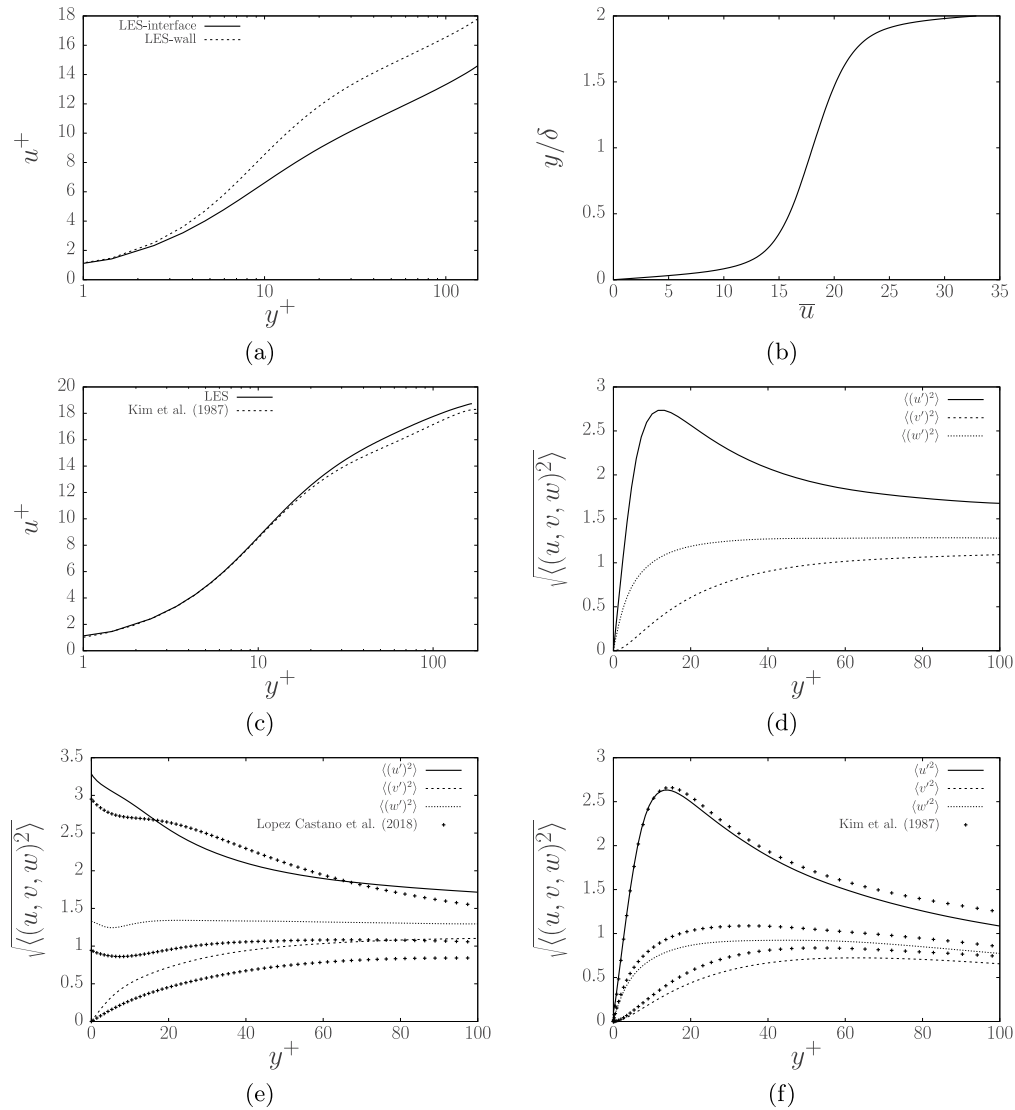


Fig. 2. Mean velocity and RMS profiles for the water and the air sub-domain. (a) semilog chart of mean streamwise velocity profile of the upper and lower halves of the water side, where the wall-like boundary layer corresponds to the bottom half of the domain; (b) streamwise velocity profile over the whole depth of the air-water domain; (c) mean streamwise velocity profile in semilog chart for the air sub-domain; (d) RMS velocity fluctuations for boundary layer at the wall in the water domain; (e) RMS velocity fluctuations of the boundary layer at the interface in the water domain; and (f) RMS velocity fluctuations in the air subdomain.

interval of 159.5 viscous time units, during which 150 independent samples were collected. The averaging process denoted by $\langle \cdot \rangle$, is defined as an averaging over the homogeneous (x, z) directions and the time samples, unless otherwise indicated. Moreover, fields obtained from the LES are denoted by $\overline{(\cdot)}$. Thus, resolved fluctuations of a certain field ϕ are defined as

$$\phi'(x, y, z) = \overline{\phi}(x, y, z) - \langle \overline{\phi} \rangle(y) \quad (9)$$

Three boundary layers are present in our problem. Two of these boundary layers are contained in the shallow water channel - where a Couette type flow develops - and the third is the boundary layer forming at the air-water interface on the air side - here a Poiseuille type flow develops. In Fig. 2 we collect a number of basic statistics characterizing the flow. These results are discussed next.

3.1.1. Mean velocity profiles

Fig. 2 a and b show the streamwise velocity profiles in the water sub-domain. These profiles have characteristics very similar to those found in Couette flow. Some subtle differences are in place, stemming from the coupling to the Poiseuille flow on top. In terms of wall-coordinates, near the interface on the water side, the boundary layer

displays a considerably thinner viscous sub-layer, compared to the classical wall boundary layer. This was also observed in Lombardi et al. (1996). Similar findings were reported in pulsating free-surface flows with constant winds (Kramer et al., 2010), and in boundary layers over wavy walls (De Angelis et al., 1996). The velocity profile corresponding to the boundary layer in the water domain, close to the interface, exhibits behaviour similar to that of a rough wall. This was also reported in Lombardi et al. (1996); Lopez Castano et al. (2018) for counter-current Poiseuille-Poiseuille flows. With respect to the velocity profile in the lower-end of the water sub-domain we observe a nearly perfect agreement with the classical boundary layers in a channel with two no-slip walls. This illustrates the modest coupling between the interfacial dynamics and the dynamics in the boundary layer near the bottom wall in the water sub-domain.

The third boundary layer in this problem, i.e., the one developing on the air side, near the interface, is considered next. The mean velocity profile is quantitatively very similar to the classical wall-bounded flows Kim et al. (1987), as seen in Fig. 2c. Here, we presented the boundary layer profile relative to the interfacial velocity U_{Γ} . Clearly, the water sub-domain presents effectively a solid wall condition to the boundary layer on the air side. Only further away from the interface

into the air domain, some differences with the classical solid wall boundary layer are observed, reflecting the fact that the upper-most boundary is represented here as a free-slip condition instead of a no-slip condition.

3.1.2. Velocity fluctuations

The root-mean-square velocity fluctuations for both air and water are presented in Fig. 2(d-e-f). We will discuss the three boundary layers separately:

- On the water side near the bottom wall the RMS velocity fluctuations are qualitatively very similar to the classical boundary layers in a no-slip channel, shown in Fig. 2d. The peak of the streamwise fluctuations takes a value ≈ 2.6 in the buffer region, which is slightly lower than the value reported for canonical wall-bounded flows, i.e., ≈ 2.8 . This can be traced back to the fact that the energy contained in the streamwise flow is redistributed over the other directions more strongly in this set-up, compared to the classical channel flow. This reduces the magnitude of the fluctuations in the streamwise velocity - we will discuss the energy redistribution in more detail momentarily.
- On the water side near the interface region, the RMS velocity fluctuations are shown in Fig. 2e. There are marked differences compared to the classical no-slip walls. For example, streamwise and spanwise fluctuations do not reduce to zero when approaching the interface. Moreover, the spanwise fluctuations of the velocity remain nearly constant at a value of ≈ 1.3 except in the buffer where a slight drop in w'_{rms} is seen. Such drop can be attributed to the production of vertical vorticity at the interface. In general, the spanwise and vertical profiles on the water side show slightly higher fluctuation levels in the core region of the flow when compared to canonical channel flows Pope (2000). The fluctuation levels are also higher than what was observed in coupled counter-gradient Poiseuille-Poiseuille flows as studied in López Castaño et al. (2018).
- The RMS of velocity fluctuations on the air sub-domain are quantitatively similar to wall-bounded flows. The profiles shown in Fig. 2f further underpin the fact that seen from the air-side the water layer acts mainly as if it was a solid no-slip wall. Note that due to the normalization of the kinematic condition 7, the root-mean-square components of the velocity at the interface present a discontinuity that scales with \mathcal{R} .

The RMS profiles shown here differ from the ones obtained in Lombardi et al. (1996) for the interface boundary layer on the water sub-domain. Turbulent horizontal mixing appears to depend to some extent on the bottom wall boundary condition. The fundamental difference between the previous study and the present simulations is the inclusion of a lower wall on the water side which, in combination with the interface, appears to increase the horizontal mixing across the channel.

We next turn to the Reynolds stress profiles in the air and water sub-domains. An expression for the shear stress τ is written as follows:

$$\frac{\tau}{(u^*)^2} = \frac{1}{Re} \frac{d\langle u^+ \rangle}{dy^+} - \frac{\langle u'v' \rangle}{(u^*)^2} \quad (10)$$

in which u^* is the shear velocity at the interface. In the air sub-domain τ varies linearly with height (a), while $\tau/(u^*)^2 = 1$ in the water sub-domain. The shear stress profiles for air and water domains are plotted in Fig. 3a and b, respectively. In the air domain the stress profiles closely resemble those observed in an open channel flow, further confirming that the air-water interface represents to close approximation a solid wall to the dynamics in the air sub-domain. In the water domain the profiles are qualitatively similar to canonical turbulent Couette flows. However, because of the differences in conditions near the bottom wall and near the interface on the water side, the Reynolds stress profile is

not symmetric about the half-height of the channel on the water side. Instead, the $\langle u'v' \rangle$ peak is closer to the interface, shifted by $y^+ \approx 100$.

The asymmetry in the Reynolds stress profile is linked to the vertical mixing across the interface, which is absent in case of a classical Couette flow. Specifically, the maximum in $\langle u'v' \rangle$ is roughly 5% higher compared to the value at the edge of the boundary layer near the wall. The asymmetry is also reflected in different thicknesses of the boundary layers near the bottom and top of the water sub-domain. Near the interface the boundary layer is thinner, implying the profile to be asymmetric at mid-height. Correspondingly, the increased Reynolds shear stress in the interface region leads to the velocity profile in Fig. 2a to display slight rough wall features. In fact, the interaction between the boundary layers on the air and on the water sides of the interface act as an additional roughness.

3.1.3. Reynolds stresses: Quadrant analysis

The asymmetry in the Reynolds stress profile in the water sub-domain reflects the interaction of this sub-domain with the air flow on top. This may be linked to flow dynamics in more detail using the so-called quadrant analysis.

Closely following Wallace (2016), the partial contributions to the Reynolds stress from each of the quadrants in the (u, v) plane, may be obtained. The resolved Reynolds stress quadrant profiles (Willmarth and Lu, 1972) in the water sub-domain and in the air sub-domain are shown in Fig. 4, averaged over $x - z$ planes. In Fig. 4a we plot the profiles for the boundary layer on the air side. These profiles are very similar to well-known findings for wall-bounded turbulence. This is consistent with the water sub-domain effectively representing a solid-wall boundary condition to the air sub-domain. This is further underpinned by the virtually indistinguishable results obtained for the solid wall boundary layer that forms at the bottom of the water sub-domain (cf. Fig. 4b). Further into the domain, turbulent intensities are in general somewhat stronger at the solid wall boundary layer compared to the air side boundary layer, especially where sweeps and ejections in quadrants II and IV are concerned. This suggests that the higher vertical mixing at the interface weakens ejection-sweep events locally. Turning to the remaining interface boundary layer in the water sub-domain, the intensity of ejections and sweeps in quadrants II and IV respectively, is slightly higher compared to the solid wall boundary layer, when $y^+ \lesssim 10$, and a little lower further out into the flow.

3.1.4. Reynolds stresses: Anisotropy invariant map

The anisotropy of the Reynolds stresses is a further expression of the type of local turbulence characteristics associated with the three boundary layers in the domain. Fig. 5 shows an Anisotropy Invariant Map (AIM) of the second and third invariants of the anisotropic Reynolds stress tensor, for the flow on the air side and the water side. Here, we denote $\eta = II^{1/2}$ in terms of the second invariant II , which is a measure for the anisotropy of the tensor, and $\xi = -III^{1/3}$ in terms of the third invariant III , which characterizes the shape of the tensor. The invariants (η, ξ) of the anisotropic Reynolds stress tensor trace a characteristic path within the 'Lumley triangle', i.e., the region enclosed by the solid lines in Fig. 5, marking all realizable states of the Reynolds stress tensor.

Near the interface, on the air side, a characteristic similar to that of a wall-bounded boundary layer is observed. The AIM shown in Fig. 5a indicates two well-known basic states of the Reynolds stress tensor: (1) a two-component shape, where $\langle u'u' \rangle \approx \langle w'w' \rangle > \langle v'v' \rangle$, and (2) an axisymmetric shape along the streamwise direction where $\langle u'u' \rangle > \langle w'w' \rangle \approx \langle v'v' \rangle$, seen in the graph as the points that lie on the right hand side in the Lumley triangle.

Near the interface, on the water side, slightly different Couette-type boundary layer characteristics are observed showing also a two-component shape close to the interface, and a lower maximal value of ξ , compared to a solid-wall boundary layer. We notice that the solid-wall

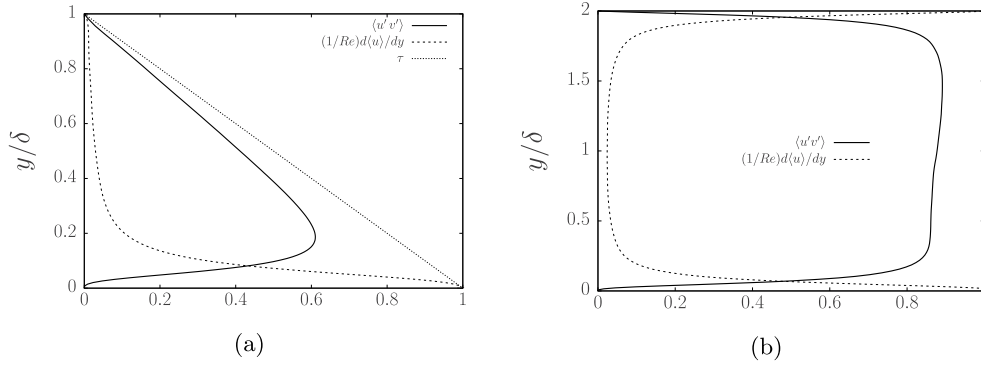


Fig. 3. Mean vertical Reynolds stress, $\langle u'v' \rangle$, profiles for the (a) air sub-domain, and (b) for the water side.

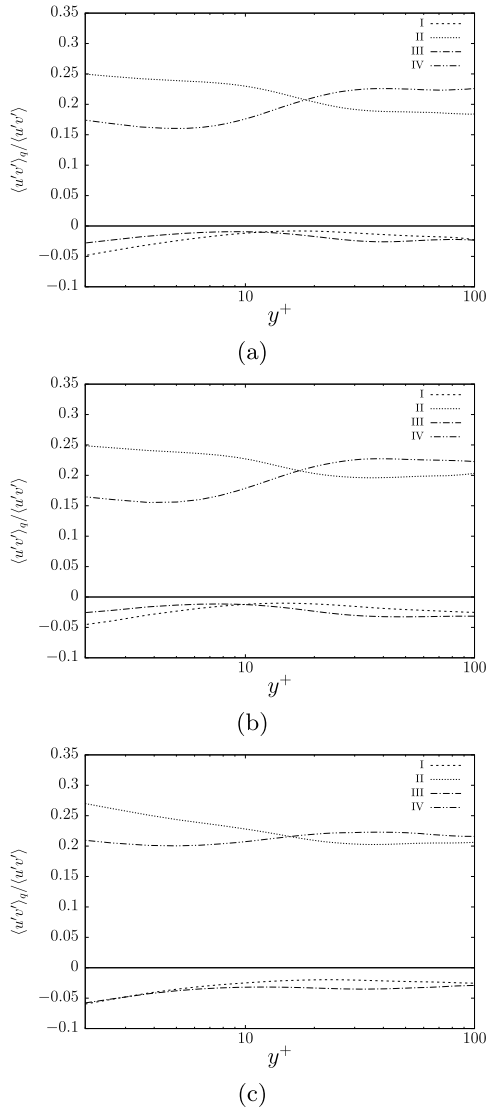


Fig. 4. Quadrant analysis of $\overline{u'v'}$ events in the Couette–Poiseuille flow for (a) the boundary layer on the air side, (b) the wall boundary layer on the water side, and (c) the interface boundary layer on the water side.

boundary layer on the water side shows slightly lower values of ξ when compared to the boundary layer on the air side.

3.1.5. Turbulent kinetic energy budget

The balance equation for the resolved turbulent kinetic energy, $k = \sqrt{u_i' u_i'}$ (TKE), in incompressible flow can be expressed as:

$$\left\langle \frac{Dk}{Dt} \right\rangle = P + \Pi_k + T_k + D_k + \epsilon = 0$$

where we introduced

$$\begin{aligned} P &= \langle u_i' u_j' \rangle \frac{\partial \langle u_i \rangle}{\partial x_j} \\ \Pi_k &= - \frac{1}{\rho} \frac{\partial \langle p' u_i' \rangle}{\partial x_i} \\ T_k &= - \frac{1}{2} \frac{\partial \langle u_i' u_i' u_j' \rangle}{\partial x_j} \\ D_k &= \frac{1}{2 Re} \frac{\partial^2 \langle u_i' u_i' \rangle}{\partial x_k \partial x_k} \\ \epsilon &= - (1/Re) \left\langle \frac{\partial u_i'}{\partial x_j} \frac{\partial u_i'}{\partial x_j} \right\rangle \end{aligned}$$

Here, use was made of the fact that the flow domain has two periodic directions. These terms, in the order presented above, are called production, pressure diffusion, turbulent transport, viscous diffusion, and dissipation of TKE. Recall that $\langle \cdot \rangle$ denotes an averaging over time and the periodic directions, (x, z) . The averaged material derivative $\langle Dk/Dt \rangle$ is zero for a fully developed turbulent flow.

In Fig. 6, the kinetic-energy balance profiles are shown for the different boundary layers present in the system. For the interface boundary layer on the water side, Fig. 6a shows an increased viscous diffusion in the region $y^+ < 10$ compared to the boundary layer that forms near the bottom wall. Similar contributions of the near-interface turbulent transport term mark a gradual departure from canonical wall-bounded turbulence and indicate a heightened mixing on a thinner boundary layer. Note that viscous diffusion is as strong as dissipation in the $15 < y^+$ range, roughly mirroring the shape of the production term. Comparing Fig. 6b and c, qualitatively similar wall-bounded boundary layer features are clear, while the peaks of TKE production and viscous dissipation are slightly closer to the interface on the air side, while dissipation shows a peak at $y^+ \approx 3$.

Although statistical self-similarity in the log-region is difficult to determine for low-Reynolds number flows, some interesting features can be observed from the production-to-dissipation ratio, P/ϵ . From Fig. 7a, it appears that the flow is approximately self-similar in the region $y^+ > 20$ with a ratio $P/\epsilon \approx 1.4$ and a maximum of ≈ 1.6 near the interface. Note that for Reynolds-Averaged turbulence modeling, this ratio is assumed equal to one, as supported by DNS and experimental results on high-Reynolds channel flows. For low Reynolds number air-water interfaces it appears that models should take a higher ratio into account. Fig. 7b for the boundary layer near the solid wall on the water side shows slightly higher values in the $y^+ > 20$ region, reaching also $P/\epsilon \rightarrow 1.4$ near the center of the water layer. Finally, Fig. 7c shows considerable differences and no apparent asymptote on the air side. This is consistent with DNS experiments (Pope, 2000) for

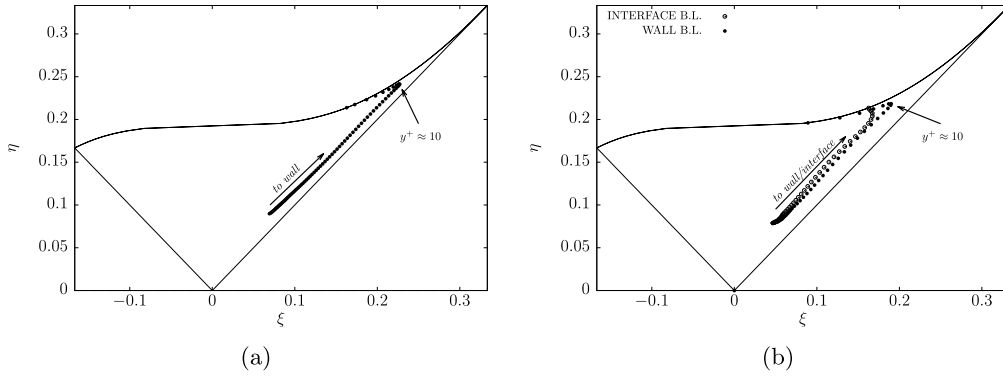


Fig. 5. Lumley triangle for the flow on (a) the air side, and (b) the water side.

low-Reynolds number channel flows.

3.2. Turbulent Reynolds stress budget

The transport equations for the resolved Reynolds stresses can be derived from the incompressible Navier–Stokes equations. The generic transport equation can be written as:

$$\begin{aligned} \frac{D\langle u'_i u'_j \rangle}{Dt} = & - \left(\langle u'_i u'_k \rangle \frac{\partial \langle u_j \rangle}{\partial x_k} + \langle u'_j u'_k \rangle \frac{\partial \langle u_i \rangle}{\partial x_k} \right) - \frac{1}{\rho} \left\langle u'_i \frac{\partial p}{\partial x_j} + u'_j \frac{\partial p}{\partial x_i} \right\rangle \\ & - \frac{\partial}{\partial x_k} \langle u'_i u'_j u'_k \rangle \\ & + \nu \frac{\partial^2}{\partial x_k^2} \langle u'_i u'_j \rangle - 2\nu \left\langle \frac{\partial u'_i}{\partial x_k} \frac{\partial u'_j}{\partial x_k} \right\rangle \end{aligned} \quad (11)$$

The terms on the right hand side are respectively the production, pressure diffusion, turbulent transport, viscous diffusion, and dissipation, ϵ_{ij} . An important term is the pressure diffusion, which acts both as a source of energy and as a mechanism of redistribution of shear

Reynolds stress. This term can be further decomposed as follows:

$$\Pi_{ij} = \frac{p'}{\rho} \left\langle \frac{\partial u'_i}{\partial x_j} + \frac{\partial u'_j}{\partial x_i} \right\rangle - \frac{\partial}{\partial x_k} \left\langle \frac{p'}{\rho} (u'_i \delta_{jk} + u'_j \delta_{ik}) \right\rangle = \langle \mathcal{R}_{ij} \rangle - \langle \mathcal{T}_{ijk} \rangle \quad (12)$$

where \mathcal{R}_{ij} indicates the pressure-rate-of-strain tensor which redistributes energy towards isotropy of turbulence. Note that the pressure-transport term, \mathcal{T}_{ijk} , is a conserved quantity whereas \mathcal{R}_{ij} represents a source/sink of Reynolds stress.

The trace of \mathcal{R}_{ij} is conserved by virtue of mass conservation, that is, $\sum_{i=1}^3 \mathcal{R}_{ii} = 0$. Each of the elements in the diagonal of \mathcal{R}_{ij} represents a source/sink for the other two elements. The diagonal elements, called pressure-strain correlation terms, can be written as:

$$\mathcal{R}_{ii} = \frac{1}{\rho} \left\langle p' \frac{\partial u'_i}{\partial x_i} \right\rangle \quad (13)$$

where a positive value of \mathcal{R}_{ii} implies a transfer of energy to one component from the other two components, and when it is negative the transfer is opposite.

In the case of the interface boundary layer on the water side Fig. 8a

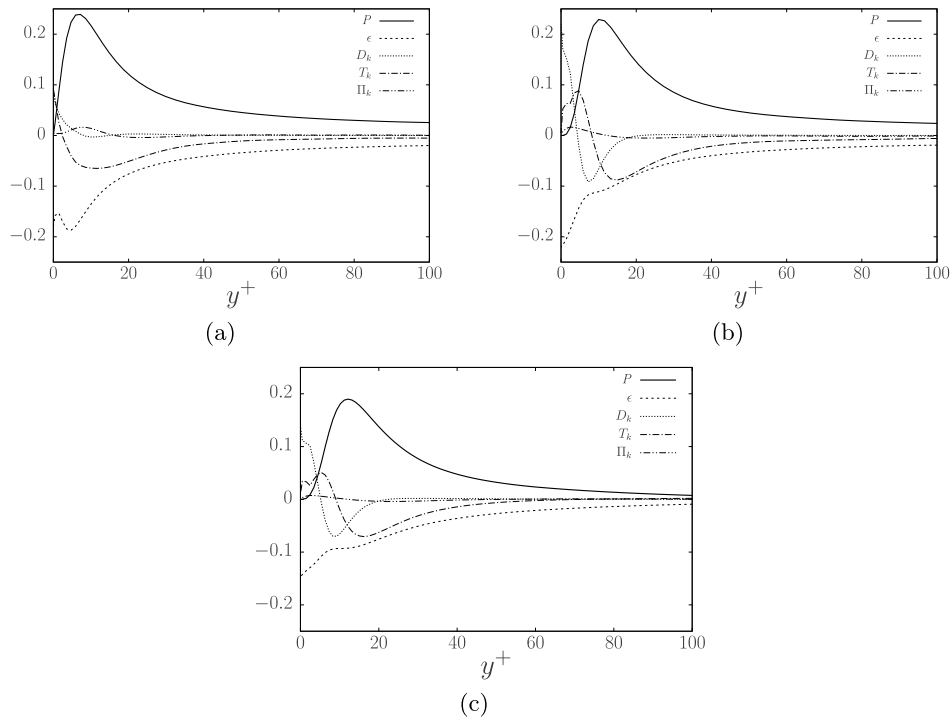


Fig. 6. Profiles of TKE for (a) the interface boundary layer on the water side, (b) the wall boundary layer at the bottom wall, and (c) the interface boundary layer on the air side.

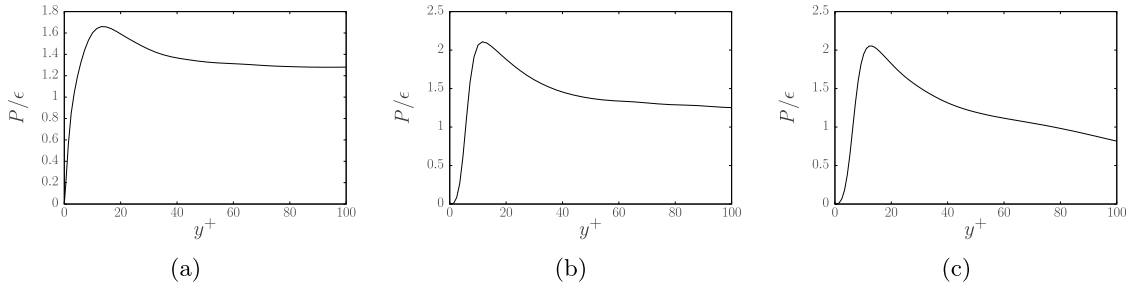


Fig. 7. Profiles of P/ϵ for (a) the interface boundary layer on the water side, (b) the wall boundary layer near the bottom wall, and (c) the interface boundary layer on the air side.

shows energy is being drained from both the vertical and the streamwise directions to the spanwise direction, for $y^+ < 10$. As previously mentioned, platts originated in the buffer region of the interface boundary layers in either water or in air redistribute energy towards the spanwise direction, in the near interface region. Whether such events happen simultaneously on both sides of the interface, and at what intensity, will be analyzed in later sections. Fig. 8b and c are very similar to each other, both representing effectively a solid wall boundary layer. The boundary layer on the air side shows a slightly stronger redistribution compared to the wall boundary layer located on the water side. Energy draining on the streamwise direction is roughly nil for the latter two cases, in contrast to the dynamics at the interface boundary layer on the water side.

3.3. Higher order statistics on the water side

The flatness factor F of the fluctuating velocities (u' , w' , v') in the coupled Poiseuille-Couette system is presented in Fig. 9. The intermittency of streamwise velocity fluctuations at the interface on the shallow water side is lower than 3, implying less extreme events in that particular direction. Furthermore, the kurtosis on the streamwise direction in all cases show a minimum between $10 < y^+ < 11$, in the region where the maximum production of TKE lies. Unlike wall-bounded turbulence the peak of spanwise and vertical flatness factors shown in Fig. 9a and c are not at $y^+ \leftarrow 0$, indicating some form damping induced by the interface. Note that no such damping in the spanwise and vertical kurtosis profiles are present near the wall on the channel, as it seen in Fig. 9b.

3.4. Two-point correlations

The two-point temporal correlation coefficients of the streamwise velocity fluctuation, u , is determined using the following estimator

$$R_{uu}(\mathbf{x}, t) = \frac{1}{N} \sum_{j=1}^N \frac{u(\mathbf{x}, t)u(\mathbf{x}, t + j\Delta t)}{(u_{rms})^2} \quad (14)$$

in which $\Delta t = 1 \times 10^{-4}$ and N the total number of samples taken over a period of 159 eddy turnover times. In Fig. 10 the two-point correlation

for the sum $R_{uu} + R_{vv} + R_{ww}$ is presented for horizontal planes located at heights $y^+ = 8.65$ measured from the nearest boundary parallel to such plane. Previous studies on Couette flow Lee and Kim (1991); Bech et al. (1995) have used this quantity to determine the ‘marginality’ of the outer spatial scales for the simulation, using the height just proposed. Such marginality was described as the possibility of obtaining two different turbulent flow realizations: ‘periodic’ or ‘disordered’, depending on whether large-scale structures have ‘sufficient room’ to develop. In this particular study, horizontal scales were chosen to be at least double those used in recent DNS experiments (Lombardi et al., 1996; Liu et al., 2009; Kurose et al., 1996; Fulgosi et al., 2003). Fig. 10a and b show significant positive correlation contours crossing the periodic boundaries indicating the solution to be in the ‘periodic’ state.

3.5. ERCP and DRCP on the water side

The modified properties of the comprising fluids, air and water, used in the ERCP case are shown in Table 1. As mentioned earlier, by using the standard properties of air and water (at 293 K) one imposes a ratio between the *shear Reynolds numbers* in the air and water sub-domains of about 2.2, as selected in the DRCP case. Previous Authors (Lombardi et al., 1996; Komori et al., 1993; Lopez Castano et al., 2018) have hypothesized about the effects of such assumption, but no comparative analysis has been made. This Subsection addresses the issue and compares simulation predictions of both settings.

The increase in the shear Reynolds number on the air side for DRCP compared to ERCP brings about some small quantitative differences, as seen in Fig. 11a. The velocity-defect ΔU (≈ 2.1) of the interface boundary layer on the air side is slightly higher than in the ERCP setting. Moreover, the RMS stresses remain roughly unchanged between DRCP and ERCP, despite the increase in $Re_{\tau,air}$, as seen in Fig. 11b. Finally, consider that the air-to-channel mean velocity ratio for ERCP is equal to $17.1/17.94 = 0.95$, whereas for the DRCP case such ratio increases to $19.59/16.6 = 1.18$, that is, an increase in the ratio between the different types of flows is of around 20%. Such is the only strong difference seen in the first and second order statistics.

The turbulent kinetic energy budget in the DRCP case is shown in

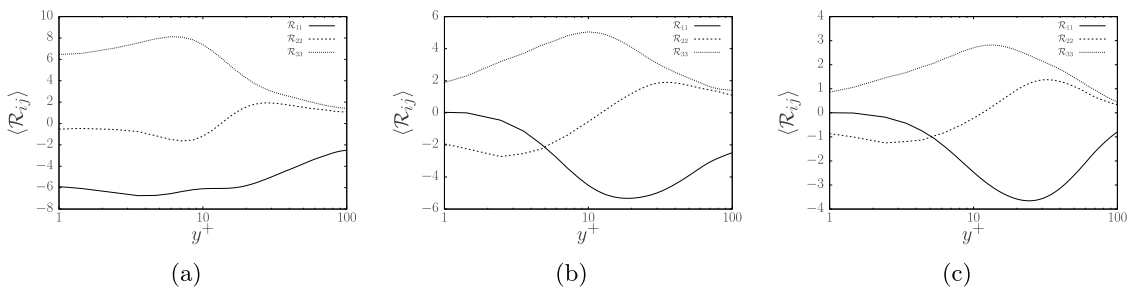


Fig. 8. Profiles of R_{ij} in the water side for (a) the interface boundary layer, (b) the wall boundary layer, and (c) the interface boundary layer on the air side, which is qualitatively similar to wall-bounded turbulence.

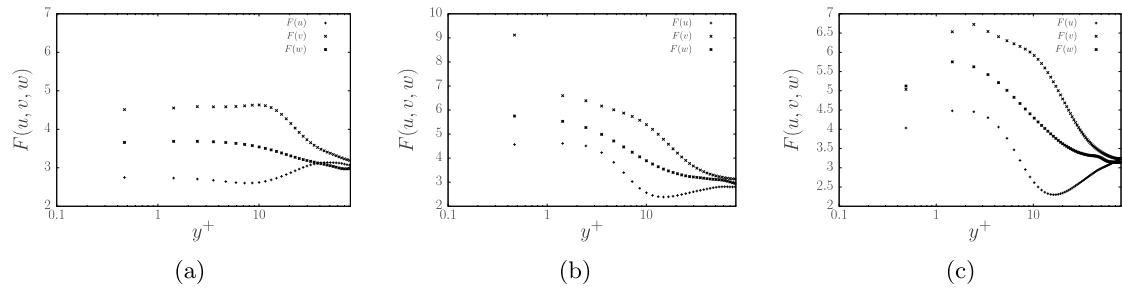


Fig. 9. Mean vertical flatness on (a) the interface boundary layer on the water side, (b) the wall boundary layer on the water side, and (c) the boundary layer on the air side.

Fig. 12a. There is a slight decrease in production and, by consequence, an increase in dissipation in DRCP when compared to the ERCF profiles of **Fig. 6a**. In general, the TKE budget is very similar for both ERCF and DRCP. Considering the pressure redistribution term shown in **Fig. 12b**, it is seen that the mechanism of energy transfer deduced from **Fig. 8a** is the same for both ERCF and DRCP.

Thus, with respect to first- and second-order statistics the ERCF simulations render similar results as the, strictly speaking, more realistic setting in DRCP. This could have been motivated intuitively beforehand - the quantification of the level of agreement that actually arises is further justification for using the computationally less expensive ERCF in this paper.

4. Vorticity dynamics

In this section, a statistical study of vorticity dynamics is made. Following the seminal work of [Fulgosi et al. \(2003\)](#), first- and second-order statistics of vorticity will be shown. Complementary to this, histograms of vortex inclination angles at the interface and at the wall are presented, following the work of [Moin and Kim \(1985\)](#). The plane locations for the latter two are in correspondence to those selected in the previously mentioned works. Finally, conditionally averaged planes of highly variable vertical vorticity in the near interface region are presented and its structure studied.

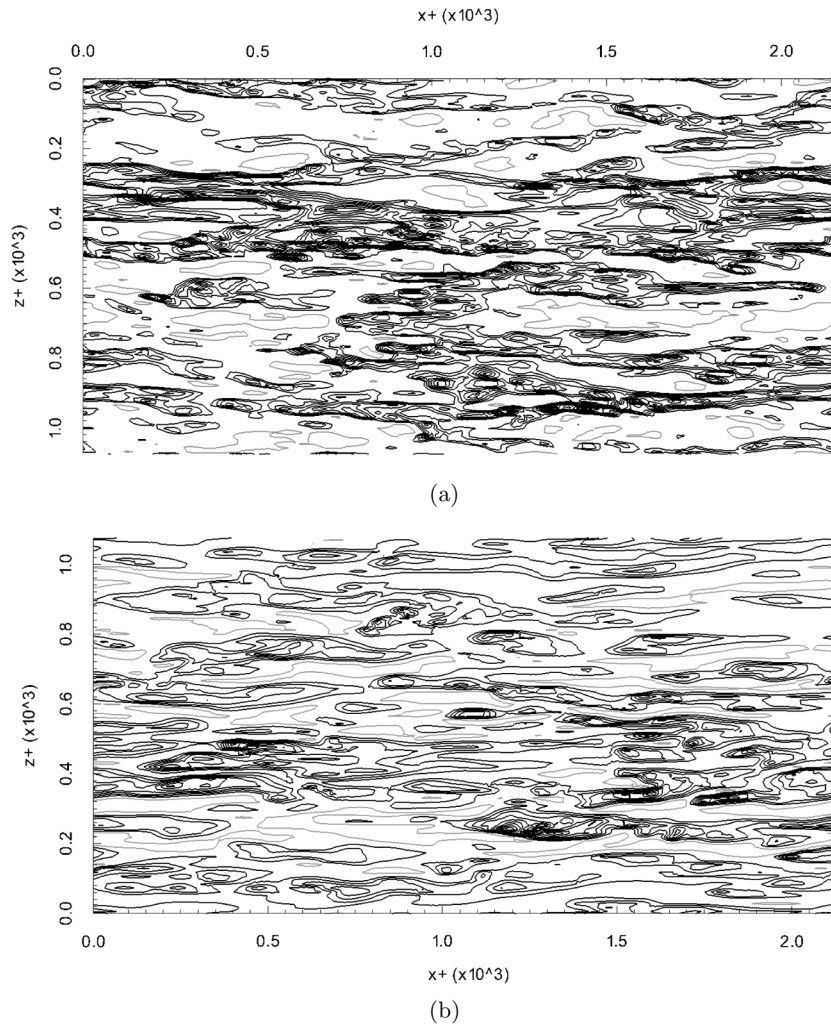


Fig. 10. Contours of the two-point velocity correlation coefficient on the water side at $y^+ = 8.65$ off the interface (a), and off the wall (b). The grey contours represent negative correlation coefficients.

Table 1Properties of air and water at $T = 320\text{ K}$ used for the ERCP case.

	Grid Dimensions	Density (m^3/s)	Kin. Visc. ($\times 10^{-6}\text{ m}^2/\text{s}$)	Dyn. Visc. ($\times 10^{-6}\text{ kg/m}\cdot\text{s}$)
Air (Upper)	$128 \times 96 \times 96$	1.08	18.11	19.62
Water (Lower)	$128 \times 96 \times 96$	988.92	0.57	56.60

4.1. First and second order statistics

The coupling between the air and water domains yields a non-zero interface-normal vorticity component, by virtue of the kinematic condition described in (7). In Fig. 13a and b, the profiles of the mean vertical vorticity components on the air and the water side are shown with characteristic high values in the boundary layers. When crossing the air-water interface, a jump in the mean vorticity appears from a value of about 0.5 on the air side to a value of about 0.35 on the water side. This is due to the scaling with different u_* on both sides, since in actual fact, the non-normalized values depend continuously on y . The RMS of vorticity fluctuations on the air and on the water sides is shown in Fig. 13c and d respectively, where likewise characteristic boundary layer profiles are seen.

4.1.1. Vortex inclination near the interface on the water side

Vortex cores near the interface on the water side show a marked inclination. This is well illustrated by histograms of vortex inclination angles, as introduced by Moin and Kim (1985), and defined in Fig. 1. We observe a strong similarity between the solid bottom wall and the interface boundary layers where the statistics of θ_{xz} is concerned (Cf. Fig. 14a and c). Conversely, the histograms representing the projection

of the vorticity vector on the xy -plane show strong qualitative differences (Cf. Fig. 14a and c). In fact, near the interface the vortices have inclination angles that strongly peak in the ranges between $(335^\circ, 35^\circ)$ and $(145^\circ, 205^\circ)$ while quasi-streamwise vortices are not abundant, having about half the probability of arise. On the other hand, the histogram for θ_{yx} on the wall side has a significant mode in the range $(260^\circ, 280^\circ)$, which corresponds uniquely to quasi-streamwise vortices. Previously, Liu et al. (2009) also reported this difference in vorticity alignment between wall and interface. In conclusion, although the air-water interface has many features in common with a solid wall boundary, the alignment of vortices in the corresponding boundary layers shows clear differences.

4.2. Vertical vorticity spots detected by VISA scheme

In order to visualize the spatial structure of the vertical vorticity in the near-interface and near-wall region of the water subdomain, the Variable Interval Space Averaging (VISA) technique of Blackwelder and Kaplan (2003) was employed. Such technique should offer visual aid for the understanding of increased mixing in the shallow water channel, via ejection of oblique vortices into the core region of the flow. VISA detects an event when the local variance of a variable ϕ is higher than some value. The variance σ_c of a variable $\phi(x, y, z, t)$ is defined as:

$$\sigma_c(y, t) = \frac{1}{\langle \phi^2 \rangle} \left[\frac{1}{L} \int_{-L/2}^{L/2} \phi^2 dx dz - \left(\frac{1}{L} \int_{-L/2}^{L/2} \phi dx dz \right)^2 \right] \quad (15)$$

and yields a profile as function of y for any location (x, z) . An averaging window of $2L = (\Delta x^+, \Delta z^+) \approx 170$ is used for the calculation of the variance. In VISA a further conditional averaging of σ_c over time is carried out subsequently, in which a detection (or weighing) function is

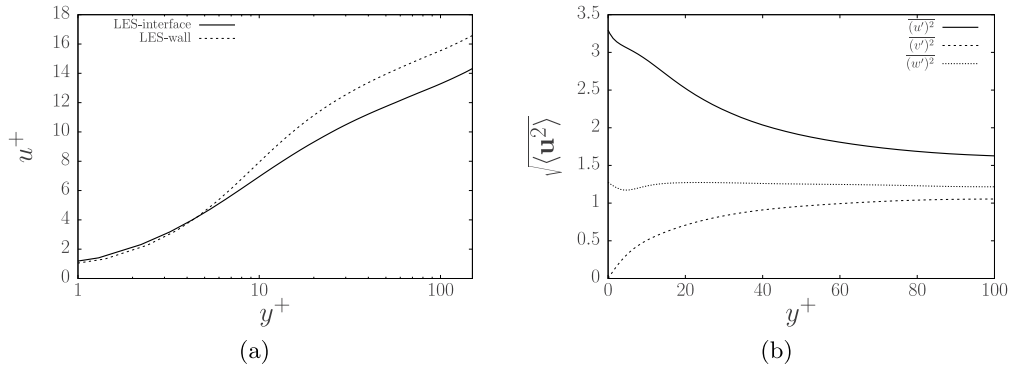


Fig. 11. DRCP Profiles on the water side: (a) velocity profile in inner scales, (b) the root-mean-square of velocities on the interface boundary layer.

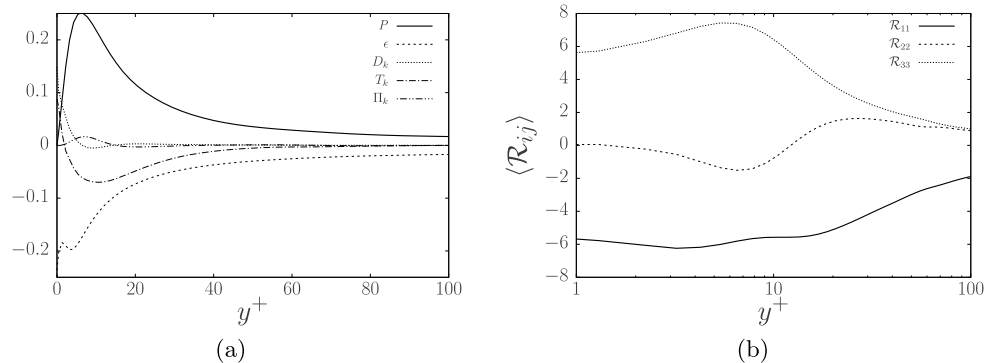


Fig. 12. DRCP budget Profiles on the water side for the interface boundary layer: (a) turbulence kinetic energy, (b) pressure redistribution term of the Reynolds stress budget.

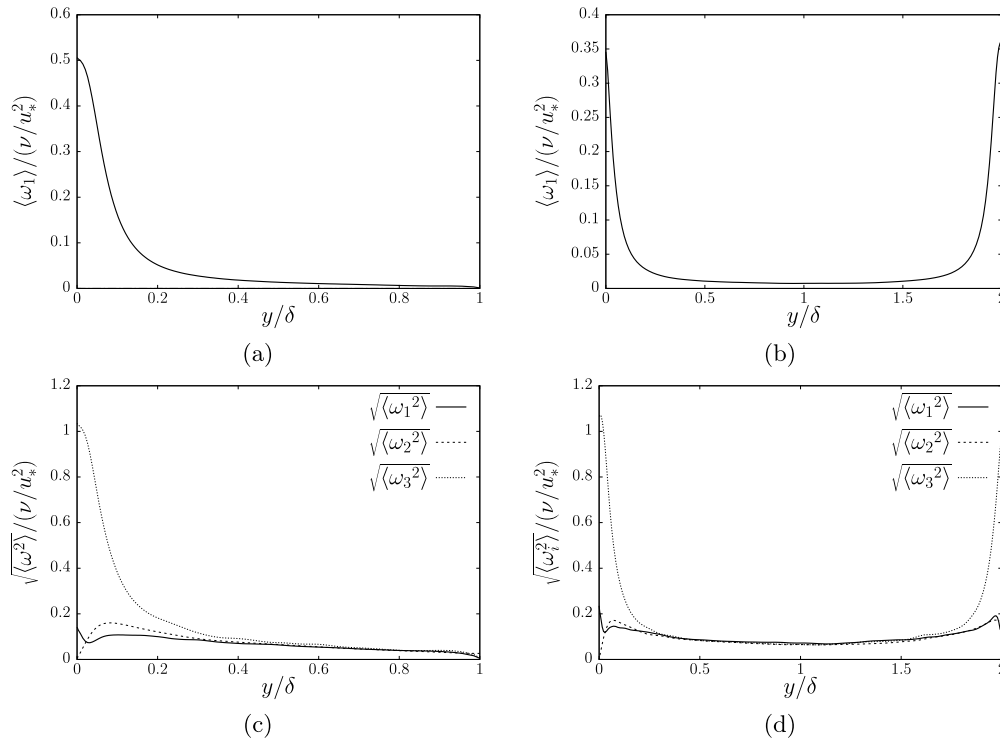


Fig. 13. Mean vorticity profile on (a) the air side, and (b) the water side. Vorticity RMS profiles on (c) the air side, and (d) on the water side.

used. The corresponding average is denoted by the symbol $\langle (\cdot) \rangle_c$. In this case, the detection of highly variable events occurring on regions of back-flow is of interest. Correspondingly, the detection function is constructed as:

$$\mathcal{D}(x, y, z, t) = \begin{cases} 1 & \sigma_c \geq 1, \frac{du}{dy} < 0 \\ 0 & \text{otherwise} \end{cases} \quad (16)$$

extracting intense events ($\sigma_c > 1$) in back-flow regions $du/dy < 0$.

In Fig. 15 a plane located at $y^+ \approx 7$ containing contours of the conditionally-averaged vertical vorticity is shown. The selected location is near the location of maximal RMS of vertical vorticity. Previous observations on wall-bounded channel flow [Lenaers et al. \(2012\)](#) have shown that backflow events extend up to $y^+ = 4.5$. In the present case, it is clear that the impingement of oblique vortices in the water sub-domain near the air-water interface is commonplace showing a much deeper penetration compared to standard channel flow. In fact, in Fig. 15a large regions of positive vertical vorticity are seen to cover the plane, organized in small ‘islands’ that are convected with the flow and coalesce with other regions of positive vorticity. This is quite different from the dynamics near the bottom wall where much lower values arise that are also less dynamic because of the low convection velocity.

5. Conclusions

The calculations presented here have demonstrated that the coupled interaction of air flow with a shallow water channel cannot be reduced to its parametrization via mean wind stress: the formation of an interfacial boundary layer on the water side is in place, even for low Re . Such interfacial boundary layer differs significantly from boundary layers driven by moving plates or boundary stress, in that velocities and turbulence intensities for Couette flows differ from the present results. On the air side, the disparity in densities guarantees a wall-like behavior of the air side which leads to results very similar to classical turbulent Poiseuille flows.

In particular the profile of *Reynolds stress* along the water side shows a non-negligible asymmetry, locating the peak close to the interface.

This increased vertical mixing in the interface boundary layer exists only in cases where the present coupled approach is considered ([Lopez Castano et al., 2018](#); [Lombardi et al., 1996](#); [Kurose et al., 1996](#)), consequence the non-linear interaction between the flows across the interface. A quadrant analysis on the Reynolds stress shows that such non-linear interaction manifests in increased sweeps and ejections in the near interface region.

The increased turbulent intensities present at the interface on the water side call for a redistribution of turbulent kinetic energy different from classical wall boundary layers, which may be tied to the presence of inclined coherent structures formed across the air-water interface ([Liu et al., 2009](#)). An analysis of the pressure-strain term shows that the interface boundary layer drains energy from both the streamwise and spanwise directions, to the vertical direction, explaining the increased vertical mixing. Such behavior may be explained by the presence of inclined and energy-carrying vortex rolls formed at the interface. An analysis on the near-interface inclination of vorticity, and the detection of energy-carrying vertical vorticity spots using VISA, partially support this notion. However, future works may focus on quantifying the energy carried by such structures and its relation to vertical mixing.

The present work has considered the interface to be flat: natural consequence of effect of non-linear, non-breaking, waves is to increase the Reynolds stress as a direct results of increased form drag ([Guo and Shen, 2013](#)). Future works may consider the effect of non-breaking waves either by using *Arbitrary Lagrangian-Eulerian* methods or by means of a vortex force in the predictor equation.

Finally, the present approach has shown to be a reliable tool for the study of coupled non-mixed fluid flows sharing a flat interface. One of the main challenges facing studies of this sort is the disparity in the properties of the comprising fluids which may lead to very high difference in Reynolds Numbers between the sub-domains. One way to tackle such problem, in the case of air and water, is to artificially increase the ambient temperature (to synthetically change density and viscosity) in order to force the Reynolds number to be equal in both flows (ERPC). Here, it has been shown that mean quantities such as velocity profiles remains qualitatively similar in the case where

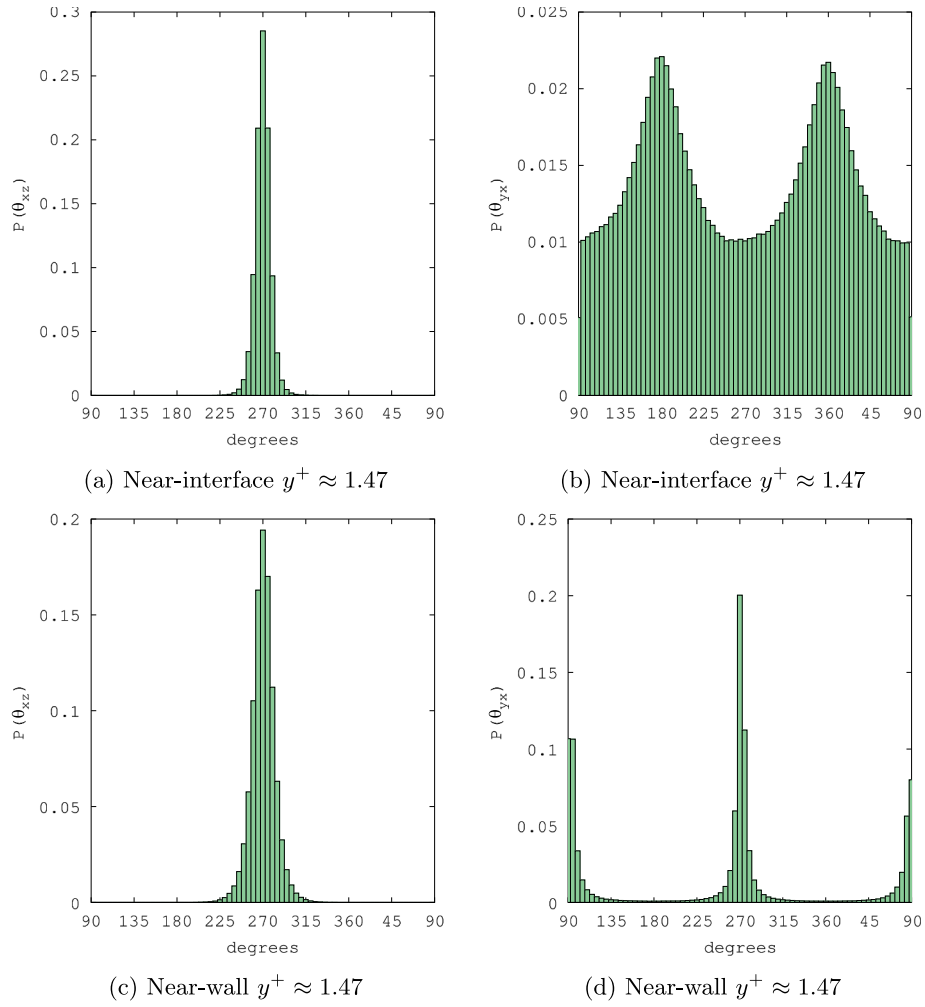


Fig. 14. Histograms of near-interface two-dimensional vortex inclination angles on the water side near the interface ((a) and (b)) and near the bottom wall ((c) and (d)). We show θ_{xz} in (a) and (c) and θ_{yz} in (b) and (d).

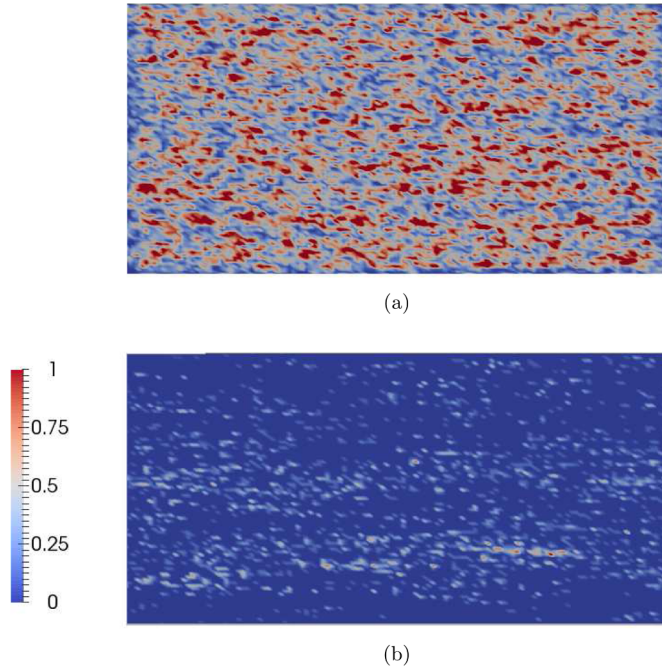


Fig. 15. Conditional average $\langle \bar{\omega}_y \rangle_c$ at $y^+ = 6.84$ off (a) the interface, and off (b) the wall in the water subdomain.

standard properties are used and where the aforementioned assumption is made. More importantly, it has been shown that the energy redistribution mechanism, studied via the pressure-strain term's components of the Reynolds stress budget, remains qualitatively similar in both scenarios indicating that the phenomena leading to increased mixing is insensitive to scaling. Nevertheless, the present work shows that the turbulent kinetic energy budget is not insensitive to the ERPC scaling close to the interface, in particular there is an increased transport of TKE away from the buffer region in the ERPC scenario. In the future, an in-depth analysis on the viability of such assumption should be made for a broader range of flows and Reynolds numbers.

Declaration of Competing Interest

All authors have participated in (a) conception and design, or analysis and interpretation of the data; (b) drafting the article or revising it critically for important intellectual content; and (c) approval of the final version.

This manuscript has not been submitted to, nor is under review at, another journal or other publishing venue.

The authors have no affiliation with any organization with a direct or indirect financial interest in the subject matter discussed in the manuscript

CRediT authorship contribution statement

Santiago López Castaño: Conceptualization, Software, Methodology, Formal analysis, Writing - original draft. **Bernard J. Geurts:** Conceptualization, Writing - review & editing, Visualization, Supervision. **Vincenzo Armenio:** Supervision, Funding acquisition, Writing - review & editing, Resources.

References

- Armenio, V., Piomelli, U., 2000. A lagrangian mixed subgrid-scale model in generalized coordinates. *Flow Turbul. Combust.* 65, 51–81.
- Armenio, V., Sarkar, S., 2002. An investigation of stably stratified flows using large-eddy simulation. *J. Fluid Mech.* 459, 1–42.
- Bech, K.H., Tillmark, N., Alfredsson, P.H., Andersson, H.I., 1995. An investigation of turbulent plane Couette flow at low Reynolds numbers. *J. Fluid Mech.* 286, 291–325.
- Blackwelder, R.F., Kaplan, R.E., 2003. On the wall structure of the turbulent boundary layer. *J. Fluid Mech.* 76.
- Craik, A.D.D., Leibovich, R., 1976. A rational model for langmuir circulations. *J. Fluid Mech.* 73, 401–426.
- De Angelis, V., Lombardi, P., Banerjee, S., 1996. Direct numerical simulation of turbulent flow over a wavy wall. *Phys. Fluids* 9 (8), 2429–2442.
- Fulgosi, M., Lakehal, D., Banerjee, S., De Angelis, V., 2003. Direct numerical simulation of turbulence in a sheared air-water flow with a deformable interface. *J. Fluid Mech.* 482, 319–345.
- Germano, M., 1992. Turbulence: the filtering approach. *J. Fluid Mech.* 238, 325–336.
- Guermond, J.L., Shen, J., 2003. Velocity-correction projection methods for incompressible flows. *SIAM J. Num. Anal.* 41 (1), 112–134.
- Guo, X., Shen, L., 2013. Numerical study of the effect of surface waves on turbulence underneath. part 1. mean flow and turbulence vorticity. *J. Fluid Mech.* 733, 558–587.
- Handler, R., Smith, G., Leighton, R., 2001. The thermal structure of an air–water interface at low wind speeds. *Tellus A* 53 (2), 233–244.
- Kim, J., Moin, P., Moser, R., 1987. Turbulence statistics in fully developed channel flow at low reynolds number. *J. Fluid. Mech.* 177, 133–166.
- Komori, S., Nagaosa, R., Murakami, Y., Chiba, S., Ishii, I., Kuwahara, K., 1993. Direct numerical simulation of three-dimensional open-channel flow with zero-shear gas-liquid interface. *Phys. Fluids* 5 (115).
- Kramer, W., Clercx, H., Armenio, V., 2010. Turbulent oscillating channel flow subjected to a free-surface stress. *Phys. Fluids* 22. <https://doi.org/10.1063/1.3481149>.
- Kurose, R., Takagaki, N., Kimura, A., Komori, R., 1996. Direct numerical simulation of turbulent heat transfer across a sheared wind driven gas liquid interface. *J. Fluid Mech.* 804, 646–687.
- Lee, M. J., Kim, J., 1991. The structure of turbulence in a simulated plane couette flow. *Proc. 8th Symp. Turbulent Shear Flow*, Vol. 5.
- Lenaers, P., Li, Q., Brethouwer, G., Schlatter, P., Orlu, R., 2012. Rare backflow and extreme wall normal velocity fluctuations in near wall turbulence. *Phys. Fluids* 24.
- Liu, S., Kermani, A., Shen, L., Yue, D.K.P., 2009. Investigation of coupled air-water turbulent boundary layers using direct numerical simulations. *Phys. Fluids* 21.
- Lombardi, P., De Angelis, V., Banerjee, S., 1996. Direct numerical simulation of near-interface turbulence in coupled gas-liquid flow. *Phys. Fluids* 8 (6), 1643–1665.
- Lopez Castano, S., Armenio, V., Geurts, B., 2018. An investigation of strong backflow events at the interface of air-water systems using large-eddy simulation. (In Press for *J. Turbulence*).
- Moin, P., Kim, J., 1985. The structure of the vorticity field in turbulent channel flow. part 1. Analysis of instantaneous fields and statistical correlations. *J. Fluid Mech.* 286, 155.
- Nagaosa, R., 1999. Direct numerical simulation of vortex structures and turbulent scalar transfer across a free surface in a fully developed turbulence. *Phys. Fluids* 11 (6), 1581–1595.
- Pope, S.B., 2000. *Turbulent Flows*. Cambridge University Press.
- Roman, F., Napoli, E., Milici, B., Armenio, V., 2009. An improved immersed boundary method for curvilinear grids. *Comput. fluids* 38, 1510–1527.
- Wallace, J.M., 2016. Quadrant analysis in turbulence research: history and evolution. *Ann. Rev. Fluid Mech.* 48, 131–158.
- Willmarth, W.W., Lu, S.S., 1972. Structure of the Reynolds stress near the wall. *J. Fluid. Mech.* 55, 65–92.
- Lorke, A., Wüest, A., 2003. Small-scale hydrodynamics in lakes. *Ann. Rev. Fluid Mech.* 35, 373–412.
- Zang, Y., Street, R.L., Koseff, J.R., 1994. A non-staggered grid, fractional step method for time-dependent incompressible Navier–Stokes equations in curvilinear coordinates. *J. Comp. Phys.* 114, 18–33.
- Zikanov, O., Slinn, D., Dhanak, D., 2003. Large eddy simulations of the wind-induced turbulent Ekman layer. *J. Fluid Mech.* 495, 343–368.